Chapter 6

Extending the Bandwidth of SFLs

Frequency-swept optical waveforms with large frequency chirp range (optical bandwidth) have applications in high resolution optical imaging, LIDAR and infrared and Terahertz spectroscopy. The spatial resolution of an imaging system using a chirped laser source is inversely proportional to the chirp bandwidth as per equation (5.16), and the unambiguous range of the distance measurement is governed by the coherence length of the laser. Optical ranging applications therefore benefit from rapidly tunable, wide-bandwidth, and narrow-linewidth swept-frequency optical sources. Rapidly swept laser sources with wide tuning ranges of ∼10–20 THz also find applications in swept-source optical coherence tomography (SS-OCT) [50]. We have demonstrated in chapter 5 the generation of precisely controllable optical frequency sweeps using an SCL in an optoelectronic PLL; however, the chirp bandwidth was limited to about 500 GHz by the tuning range of the single-mode SCLs used. In this chapter, we demonstrate two approaches to increase the chirp bandwidth for high-resolution imaging: (i) chirp multiplication by four-wave mixing (FWM) and (ii) multiple source- (MS-) FMCW reflectometry where measurements using distinct optical chirps are algorithmically stitched to produce a high-resolution image.

6.1   Chirp Multiplication by Four-Wave Mixing

In this section, we propose and demonstrate the doubling of the bandwidth of a chirped optical waveform by the process of FWM in a nonlinear optical medium. It

is a well-known observation [121] that the dithering of the pump signal to suppress Stimulated Brillouin Scattering (SBS) in a FWM experiment produces a broadening of the idler signal; this broadening is generally regarded as an undesirable side effect. We theoretically and experimentally demonstrate that the frequency chirp characteristics of the pump signal are faithfully reproduced in the idler, which implies that the chirp-doubled signal can be used for higher-resolution optical imaging. The effect of chromatic dispersion on the maximum achievable output bandwidth is analyzed, and a dispersion compensation technique to reduce the required input power levels is described. We show that this approach can be cascaded to achieve a geometrical increase in the output chirp bandwidth, and that the chirp bandwidth can be tripled using two chirped input fields. Finally, we present the design of a cyclical FWM "engine" to achieve large output chirp bandwidths using a single nonlinear waveguide.

6.1.1 Theory

6.1.1.1 Bandwidth-Doubling by FWM

Consider the experiment shown in figure 6.1. A chirped optical wave and a "reference" monochromatic wave are coupled together, amplified, and fed into a nonlinear optical waveguide with a large third-order nonlinear susceptibility $\chi^{(3)}$, and a relatively low group velocity dispersion (GVD) parameter D_c. Highly nonlinear fibers (HNLF), photonic crystal fibers, higher-order mode (HOM) optical fibers [122], semiconductor optical amplifiers (SOAs) [123] and integrated silicon waveguides [124] can be used to provide the necessary nonlinear susceptibility and control over the GVD. In this work, we will assume that the nonlinear medium is a highly nonlinear optical fiber. An optical filter, typically based on a diffraction grating, is used at the output to select the waveform of interest.

Let the electric fields of the chirped and the reference waves be given by

$$
\begin{aligned}
E_{ch}(z,t) &= \frac{1}{2}A_{ch}(z)\exp\left(j(\omega_0 t + \phi(t) - \beta_{ch}z)\right) + \text{c.c.}, \\
E_R(z,t) &= \frac{1}{2}A_R(z)\exp\left(j(\omega_R t - \beta_R z)\right) + \text{c.c.},
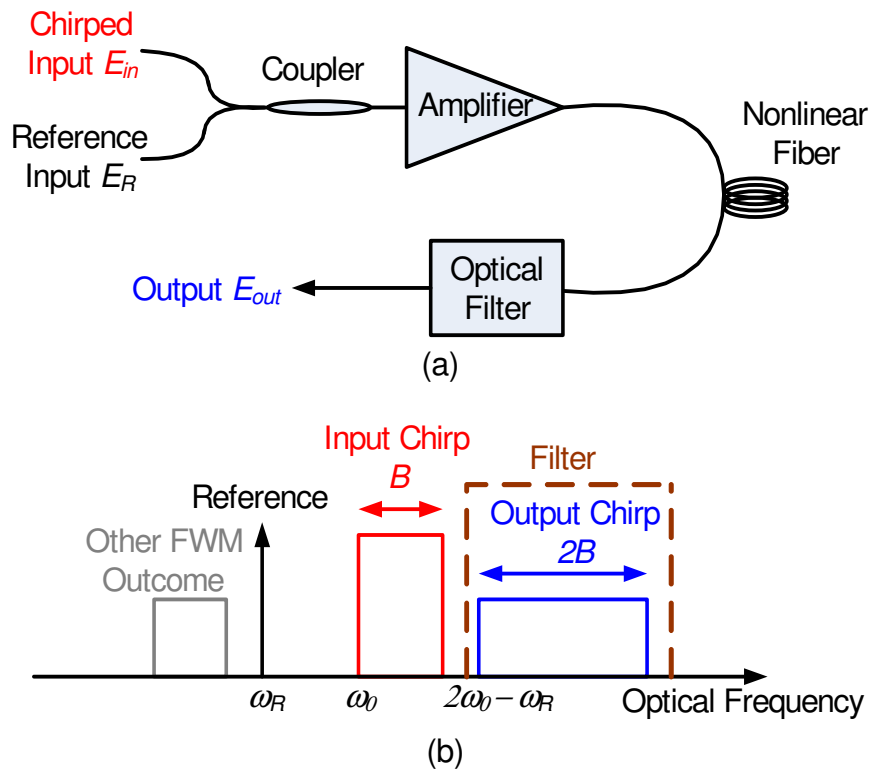\end{aligned}
\tag{6.1}
$$

Figure 6.1. (a) Schematic diagram of the four-wave mixing (FWM) experiment for chirp bandwidth-doubling. (b) Spectral components of the input and FWM-generated fields. The chirp-doubled component is optically filtered to obtain the output waveform.

where $\phi(t)$ represents the optical chirp. The fields are assumed to be linearly polarized along the same axis, and z is the direction of propagation. The propagation vectors β are determined by the waveguide. The instantaneous frequency of the chirped wave is given by

$$\omega_{ch}(t) = \omega_0 + \frac{d\phi}{dt}. \tag{6.2}$$

For the particular case of a linearly chirped wave, $\phi(t) = \xi t^2/2$, and $\omega_{ch}(t) = \omega_0 + \xi t$. Typical optical frequency chirps of interest for imaging exceed bandwidths of 100 GHz in a time less than 1 ms, and SBS effects can be neglected in this analysis. The rate of the optical chirp is several orders of magnitude slower than the optical frequency, and the chirped wave can therefore be regarded as a monochromatic wave of frequency $\omega_{ch}(t)$. The chirped and reference waves interact in the nonlinear fiber through the FWM process to give rise to a nonlinear polarization [88]

$$P_{NL} = 4\chi^{(3)} \vdots EEE, \tag{6.3}$$

where E is the vector sum of the electric fields in equation (6.1). Among the various frequency terms which are present in the triple product in equation (6.3) is the term

$$P_{NL}(z,t) \propto A_{ch}^2 A_R^* \exp\left(j\left((2\omega_0 - \omega_R)t + 2\phi(t)\right)\right), \tag{6.4}$$

which radiates a wave of frequency

$$\omega_{out}(t) = 2\omega_0 - \omega_R + 2\frac{d\phi}{dt} = 2\omega_{ch}(t) - \omega_R. \tag{6.5}$$

This process can be described quantum mechanically by the annihilation of two photons of the chirped field to create a photon of the reference field and a photon of the output field. Comparing equations (6.5) and (6.2), we see that the output chirp is twice the input chirp. By the proper selection of the input frequencies ω_0 and ω_R, the output waveform can be separated out by an optical filter, as shown in figure 6.1(b). If the bandwidth of the input chirp is B (radians), the necessary condition

for filtering the output waveform is

$$\Delta\omega(t) \doteq \omega_{ch}(t) - \omega_R \geq B. \tag{6.6}$$

Note that the output optical wavelength is in the same region as the input, and the output can therefore be amplified and reused in a cascaded scheme as discussed in section 6.1.3.

The expression for the output optical power can be obtained following a straightforward derivation [125] as outlined below. We restrict ourselves to the output electric field of the form

$$E_{out}(z,t) = \frac{1}{2}A_{out}(z)\exp\left(j(\omega_{out}t - \beta_{out}z)\right) + \text{c.c.}, \tag{6.7}$$

which is generated by plugging the nonlinear polarization in equation (6.3) into the nonlinear wave equation

$$\frac{\partial^2 E}{\partial z^2} = \frac{n^2}{c^2}\frac{\partial^2 E}{\partial t^2} + \frac{\alpha n}{c}\frac{\partial E}{\partial t} + \mu_0\frac{\partial^2 P_{NL}}{\partial t^2}, \tag{6.8}$$

where n is the refractive index in the fiber and α represents the loss per unit length. The input chirped and reference fields are assumed to be undepleted, i.e.,

$$A_{ch,R}(z) = A_{ch,R}(0)\exp(-\alpha z/2), \tag{6.9}$$

and $A_{out}(z)$ is assumed to be slowly growing along the waveguide, i.e., $\partial^2 A_{out}/\partial z^2 \ll \beta_{out}\,\partial A_{out}/\partial z$. The differential equation for the output field is then given by

$$\frac{dA_{out}}{dz} = -\frac{\alpha}{2}A_{out} - \frac{jnc\epsilon_0\gamma A_{eff}}{2}A_{ch}^2(0)A_R^*(0)e^{-3\alpha z/2}e^{-j\Delta\beta z}, \tag{6.10}$$

where A_{eff} is the effective area of the mode in the fiber, γ is the nonlinear coefficient of the fiber, given by

$$\gamma = \frac{3\omega\mu_0\chi^{(3)}}{n^2\epsilon_0 A_{eff}}, \tag{6.11}$$

and $\Delta\beta$ is the phase mismatch defined as

$$\Delta\beta \doteq 2\beta_{ch} - \beta_R - \beta_{out}. \tag{6.12}$$

The phase mismatch is a function of the frequency difference between the chirped wave and the reference wave. Ignoring the effect of self phase modulation of the chirped beam (which is valid when the input power is low), equation (6.12) can be written as

$$\Delta\beta = -2\sum_{m=1}^{\infty} \frac{\beta_{2m}}{(2m)!}(\Delta\omega)^{2m}, \tag{6.13}$$

where $\Delta\omega$ is defined in (6.6) and β_m is the mth derivative of $\beta(\omega)$, evaluated at $\omega = \omega_{ch}$. The coefficient β_2 is related to the GVD parameter D_c by $\beta_2 = -\lambda^2 D_c/(2\pi c)$.

6.1.1.2 Bandwidth Limitations due to Dispersion

The power carried by the optical wave is related to its amplitude $A(z)$ by

$$P(z) = \frac{nc\epsilon_0 A_{eff}}{2}|A(z)|^2. \tag{6.14}$$

Integrating equation (6.10), we derive the output power after propagation through a distance L [125]:

$$P_{out}(L) = \gamma^2 P_{ch}^2 P_R \, e^{-\alpha L} \left(\frac{1-e^{-\alpha L}}{\alpha}\right)^2 \frac{\alpha^2}{\alpha^2 + \Delta\beta^2} \left(1 + \frac{4e^{-\alpha L}\sin^2\frac{\Delta\beta L}{2}}{(1-e^{-\alpha L})^2}\right). \tag{6.15}$$

From equations (6.13) and (6.15), the maximum value of the input frequency separation, and hence the output chirp bandwidth, will ultimately be limited by the phase mismatch in the fiber. Consider as an example, a commercially available dispersion-flattened HNLF with a nonlinear coefficient $\gamma = 11.3$ km^{-1}W^{-1}, loss $\alpha = 1$ dB/km, and dispersion parameter $D_c = 0.5$ ps/nm.km. For this dispersion-flattened fiber, higher-order dispersion terms (β_4 and above in equation (6.13)) can be neglected. Let us assume that the chirp and reference powers are equal, i.e., $P_{ch} = P_R$. The output power as a function of the input frequency separation ($\omega_{ch} - \omega_R$), for various
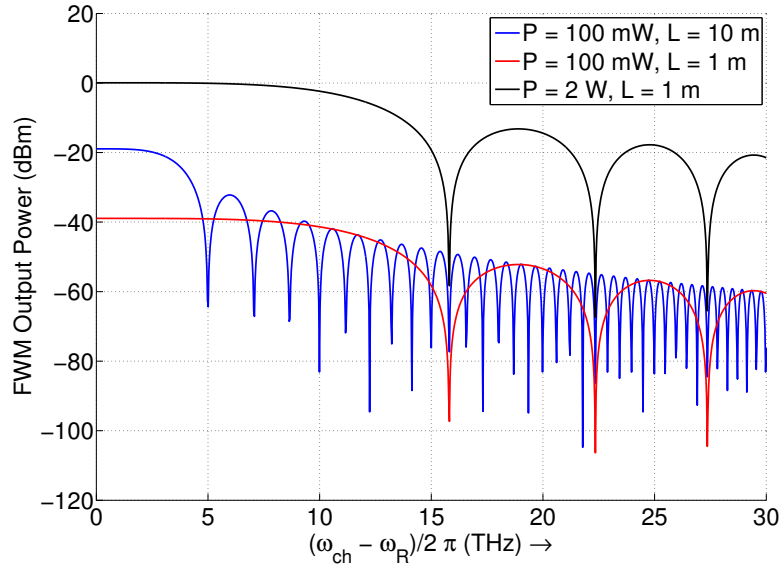
Figure 6.2. Output power as a function of the input frequency difference, for different values of fiber length and input power ($P_{ch} = P_R = P$). The dispersion, loss and nonlinear coefficient of the fiber are described in the text.

values of input power P_{ch} and fiber length L, is calculated using equations (6.13) and (6.15) and plotted in figure 6.2. The FWM bandwidth B_{FWM} can be defined as the maximum input frequency separation over which useful output power is generated, which is here taken to be the -3 dB point. It is important to note that the filtering condition in equation (6.6) implies that B_{FWM} is equal to the maximum possible output bandwidth. The maximum fiber lengths and the input power requirements for different values of output bandwidth and output power are summarized in table 6.1.

It is clear from figure 6.2 and table 6.1 that the maximum output bandwidth is determined by the length of fiber used in the experiment. For a given value of the dispersion parameter, B_{FWM} reduces as L is increased. To obtain larger bandwidths, a fiber with lower dispersion must be used. For a given length of fiber, the output power level depends only on the input power. For example, for a desired output bandwidth of 10 THz and an output power of 0 dBm, the maximum (dispersion-limited) fiber length is 1.1 m, and the input power required is $P_{ch} = P_R = 1.9$ W. This power level can be achieved with high power fiber amplifiers, but is desirable

Table 6.1. Length of HNLF and input power requirements for different output bandwidths and power levels

Output bandwidth (THz)	Maximum fiber length (m)	Input power required $P_{ch} = P_R$ (dBm)	
		$P_{out} = 0$ dBm	$P_{out} = -10$ dBm
1	105	19.5	16.2
5	4.3	29.0	25.4
10	1.1	32.8	29.5
15	0.45	35.2	32.0

that commercially available telecom-grade erbium doped fiber amplifiers (EDFAs) with output powers of approximately +20 dBm be used to reduce the system cost. In the following section, we describe a quasi-phase-matching technique using dispersion compensation to achieve this target.

6.1.1.3 Quasi-Phase-Matching Using Alternating Dispersions

It is desirable to increase the length of the nonlinear fiber used in the experiment, so as to increase the interaction length for the FWM process, thereby reducing input power requirements. However, the length cannot be increased arbitrarily, since the phase mismatch causes a reduction in the overall output power. This limitation can be overcome by using a multisegment HNLF where the sign of the dispersion parameter of a segment is alternatively chosen to be positive or negative, as shown in figure 6.3(a). The dispersion parameter D_c is changed by engineering the waveguide dispersion differently in the alternating segments. We again make the assumption of a dispersion-flattened fiber where β_4 can be neglected. Dispersion-flattened HNLFs with dispersion parameters in the range of -1.0 to +1.5 ps/nm.km at 1550 nm are readily available. An exact expression for the output field is easily obtained by integrating equation (6.10) over the entire structure (see appendix B), but we present below an intuitive explanation of the power buildup in the fiber. For a low loss fiber, we can set $\alpha = 0$

Input Optical
Waves

Nonlinear Medium

Output Wave

Dispersion: $+D_C$ $-D_C$ $+D_C$
Length: L L L

(a)

$A_{out}(L)$

$\Delta\beta = 0$

$\Delta\beta L = \pi$

Arbitrary $\Delta\beta$

Im

Re

(b)

$A_{out}(2L)$

$\Delta\beta = 0$
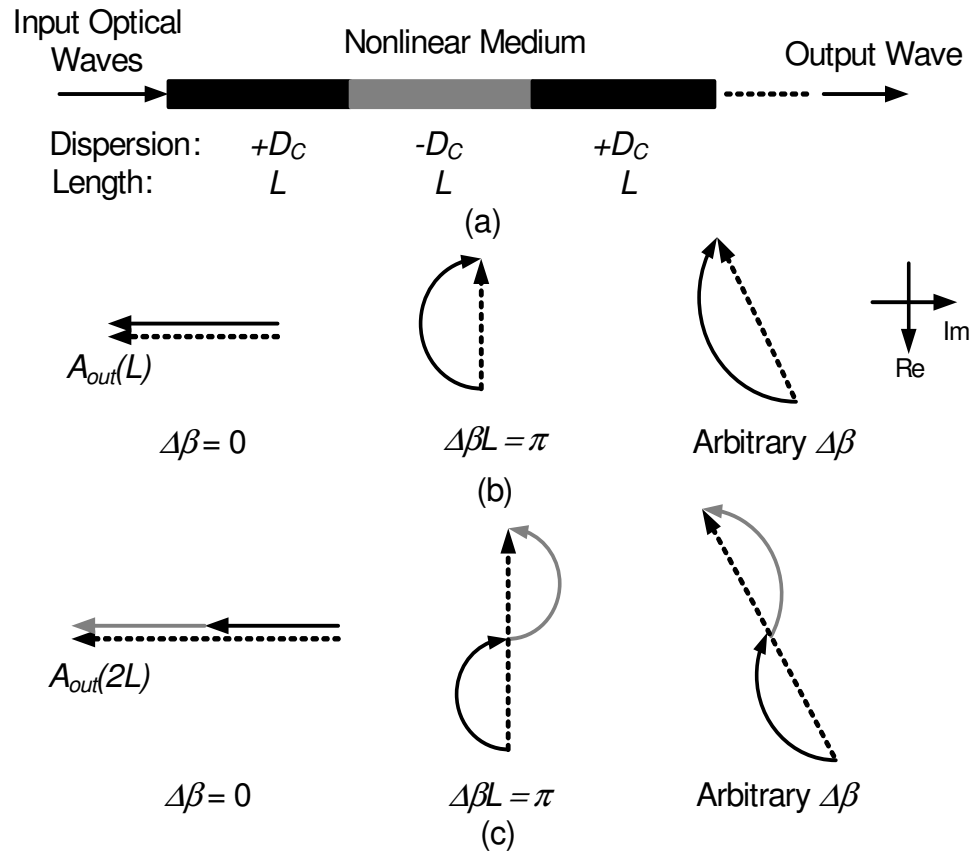
$\Delta\beta L = \pi$

Arbitrary $\Delta\beta$

(c)

Figure 6.3. (a) Multisegment alternating dispersion waveguide for quasi-phase-matching. The evolutions of the output field $A_{out}(z)$ along the waveguide for one and two segments are shown in (b) and (c) respectively. The dashed lines represent the field at (b) $z = L$ and (c) $z = 2L$.

in equation (6.10) to obtain the simple differential equation

$$\frac{dA_{out}}{dz} = -\frac{jnc\epsilon_0\gamma A_{eff}}{2}A_{ch}^2(0)A_R^*(0)e^{-j\Delta\beta z}. \tag{6.16}$$

The solution to this equation is a phasor that traces out a circle in the complex plane as the distance z is increased, as shown in figure 6.3(b). The maximum value of the field occurs when $z_{max}\Delta\beta = \pi$. As z is increased beyond this value, the magnitude of the field phasor decreases, and the power output decreases. When the sign of the dispersion parameter is reversed, the sign of $\Delta\beta$ is also reversed according to equation (6.13), and the field phasor now traces out a circle of the opposite sense, as depicted in figure 6.3(c). By symmetry considerations, the total output field at the end of the second segment is equal to twice the value of the field at the end of the first segment, *for any arbitrary value of $\Delta\beta$*. For a structure with N alternating segments, the output field scales as N, and the output power scales as N^2. The variation of P_{out} along a structure with three alternating segments of HNLF for an input frequency difference of 10 THz, calculated using equation (B.10), is plotted in figure 6.4, clearly showing the quadratic scaling of the output power with number of segments. Conversely, for a given desired output power, the input power requirement is reduced. For the HNLF example considered in section 6.1.1.2, an output bandwidth of 10 THz and output power of 0 dBm can be achieved using a structure with 30 segments of length L = 1.1 m and alternating dispersions of ±0.5 ps/nm.km, with an input power of only 200 mW, as opposed to an input power requirement of 1.9 W if a single segment were used.

The number of segments that can be used in this technique is limited by the insertion loss due to the fiber splices. Let the ratio of the transmitted to the incident field amplitudes at a fiber splice be given by t, and let $F^{(k)}$ denote the amplitude of the FWM field generated in the kth segment. The fields generated in all the segments add in phase. The chirped and reference fields in the kth segment are given by $A_{ch,R}^{(k)} = t^{k-1}A_{ch,R}^{(1)}$, and the FWM field generated in the kth segment is consequently
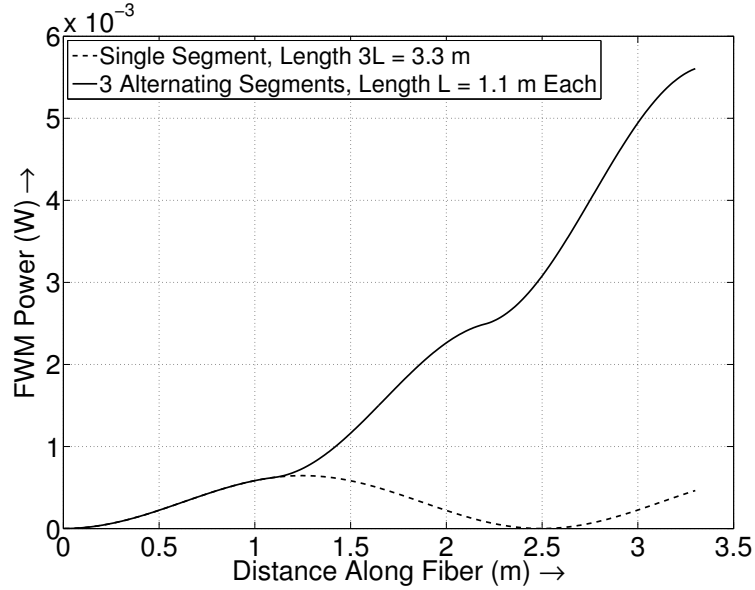
Figure 6.4. Comparison of the generated FWM field in a structure with 3 segments of lengths L each and alternating dispersions of $\pm D_c$, with a single segment of length $3L$ and dispersion $+D_c$. The values used in the calculations were $L = 1.1$ m and $D_c = 0.5$ ps/nm.km.

given by $F^{(k)} = t^{3k-3}F^{(1)}$. The output field after the kth stage is therefore given by

$$A_{out}^{(k)} = tA_{out}^{(k-1)} + t^{3k-3}F^{(1)}, \qquad (6.17)$$

which can be solved to yield

$$P_{out}^{(k)} = \left(\frac{t^{k-1}(1 - t^{2k})}{1 - t^2}\right)^2 P_{out}^{(1)}. \qquad (6.18)$$

Under the assumption that $(1 - t) \ll 1$, equation (6.18) reduces to

$$\frac{P_{out}^{(k)}}{P_{out}^{(1)}} \approx k^2 t^{2(k-1)}. \qquad (6.19)$$

It is therefore crucial to minimize the splice losses in order to increase the FWM interaction length. In the absence of splice losses, the number of segments is limited by material loss in the waveguide, and the total achievable bandwidth is ultimately limited by the gain bandwidth of the amplifiers used in the experiment.

It should be noted that quasi-phase matched FWM using a similar concept has been demonstrated theoretically and experimentally [126, 127], where the phase mismatch accumulated during the FWM process is periodically compensated for using a dispersion-compensating fiber (DCF) or a single-mode fiber (SMF). In the process described in this section, the quasi-phase-matching is achieved using nonlinear fiber. This is an important distinction since the use of SMF or DCF will require two fiber splices per segment of HNLF, which then leads to a lower achievable gain from equation (6.19). Further, the loss per splice is also expected to be higher, since dissimilar fibers have to be spliced together.

We have again neglected the effect of higher-order dispersion terms in the preceding analysis. In the presence of nonnegligible higher-order dispersion terms, perfect quasi-phase-matching can only be achieved by reversing the signs of all the terms β_{2m} in equation (6.13), for $m = 1, 2, \ldots$. However, a degree of quasi-phase-matching can still be achieved by reversing the sign of the dispersion parameter D_c. The modification to the output power due to the effect of higher-order terms can be determined exactly by integrating equation (6.10). A general expression for the power generated due to four-wave mixing in a multisegment nonlinear waveguide is derived in appendix B.

6.1.2   Experiment

6.1.2.1   Chirp Bandwidth-Doubling

A schematic diagram of the proof-of-principle experimental setup is shown in figure 6.5. The input chirped wave was a perfectly linearly chirped waveform that sweeps 100 GHz in 1 ms, generated using a DFB SCL in an optoelectronic feedback loop as described in chapter 5. A tunable laser (Agilent Technologies) was used as the monochromatic reference wave. The two optical waves were coupled using a polarization maintaining coupler, amplified using an EDFA and fed into a commercial dispersion-flattened HNLF. The HNLF had a gain $\gamma = 11.3$ km^{-1}W^{-1}, loss $\alpha = 1$ dB/km, length $L = 100$ m, and dispersion parameter $D_c = +1.2$ ps/nm.km. The
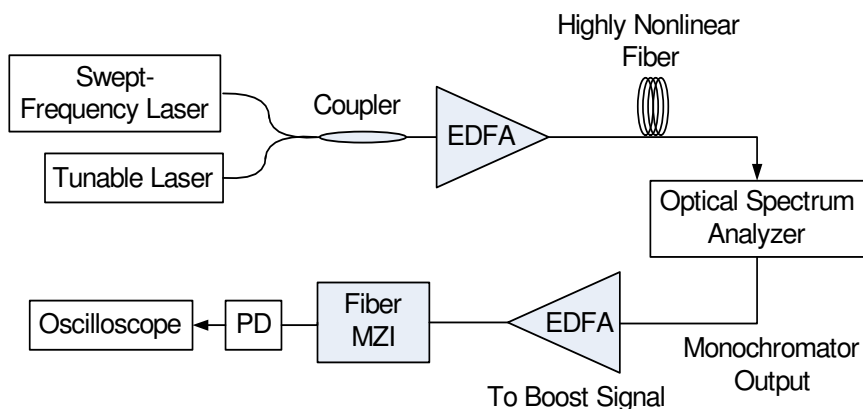
Figure 6.5. Schematic diagram of the experimental setup for the demonstration of chirp bandwidth-doubling by four-wave mixing. EDFA: Erbium doped fiber amplifier, MZI: Mach-Zehnder interferometer, PD: Photodetector. The differential delay in the MZI is approximately 2.7 ns.
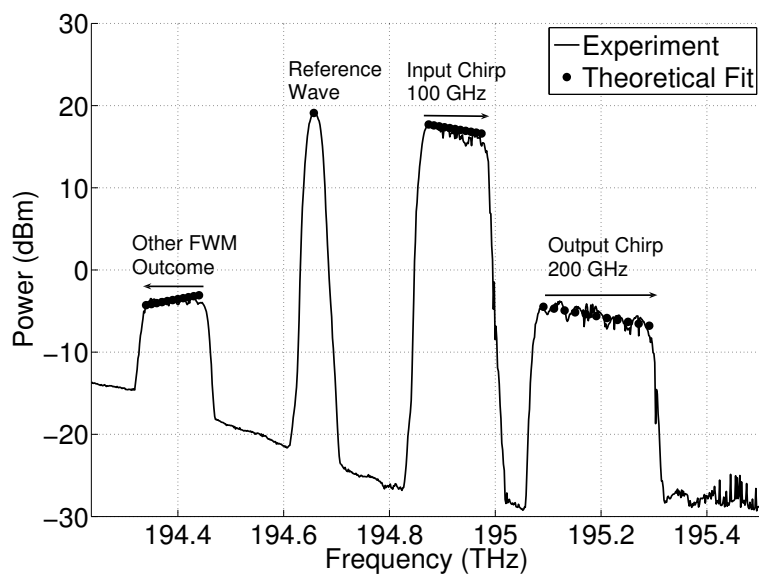

Figure 6.6. Experimental demonstration of bandwidth-doubling by four-wave mixing. The reference wave was monochromatic (resolution limited) and the input chirp bandwidth was 100 GHz. The arrows indicate the direction of the chirp. The second FWM product, generated at the lower frequency, chirps in the opposite direction. The theoretical FWM power was calculated using equations (6.13) and (6.15) using the measured input powers.

output of the HNLF was measured on an optical spectrum analyzer, and is shown in figure 6.6. The figure clearly shows the generation of a frequency doubled FWM output that sweeps over an optical bandwidth of 200 GHz. A second FWM component sweeping over 100 GHz in the reverse direction was generated on the low frequency side, corresponding to the FWM process involving two photons of the reference wave and one photon of the chirped wave. The experimentally measured values of the output fields are in excellent agreement with the theoretical calculation based on the measured input powers and equations (6.13) and (6.15).

The ability of the experiment to reproduce the dynamic characteristics of the input optical frequency chirp at the output was also verified. The output waveform was filtered out using the monochromator output of the optical spectrum analyzer, and amplified using a telecom EDFA. The input and output frequency chirps were characterized by passing them through an MZI with time delay $\tau_{MZI} = 2.7$ ns, as shown in figure 6.5. The frequency of the detected photocurrent is related to the slope ξ of the optical chirp by $\omega = \xi \tau_{MZI}$. The spectrograms of the photocurrents are calculated and plotted in figure 6.7. The results clearly show that the optical chirp rate is doubled by the FWM process from 10^{14} to 2×10^{14} Hz/s, and the transform-limited linearity of the input chirp is maintained at the output, making the output frequency chirped waveform suitable for three-dimensional imaging applications. The FWM technique can also be used to increase the chirp rate of swept frequency optical waveforms.

6.1.2.2 Dispersion Compensation

We also demonstrated improved bandwidth in the FWM process using the dispersion technique for quasi-phase-matching described in figure 6.3. Two segments of dispersion-flattened HNLF with lengths 100 m each, and dispersion coefficients +0.38 ps/nm.km and −0.59 ps/nm.km were spliced together to obtain the dispersion-compensated waveguide. The other parameters of the HNLFs were identical to the one used in the previous section. Single-mode fiber pigtails were used at the input and output ends. The results of bandwidth-doubling experiments using the individual fibers and the

Input Spectrogram (dB)

(a)

Output Spectrogram (dB)
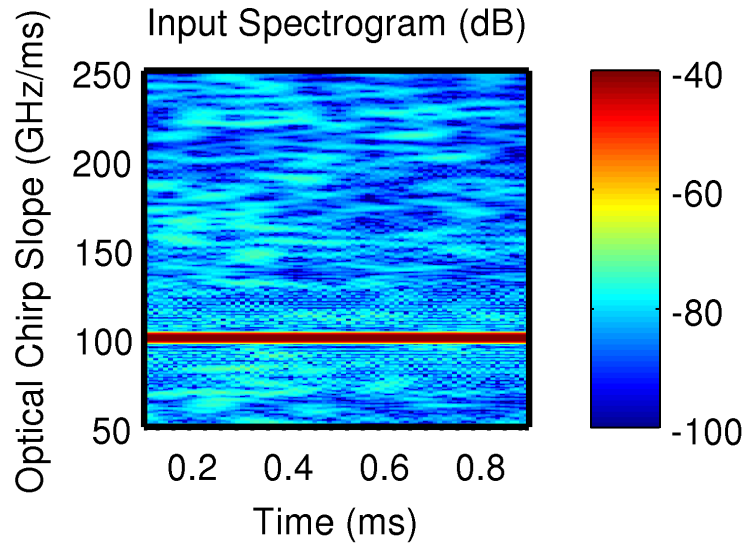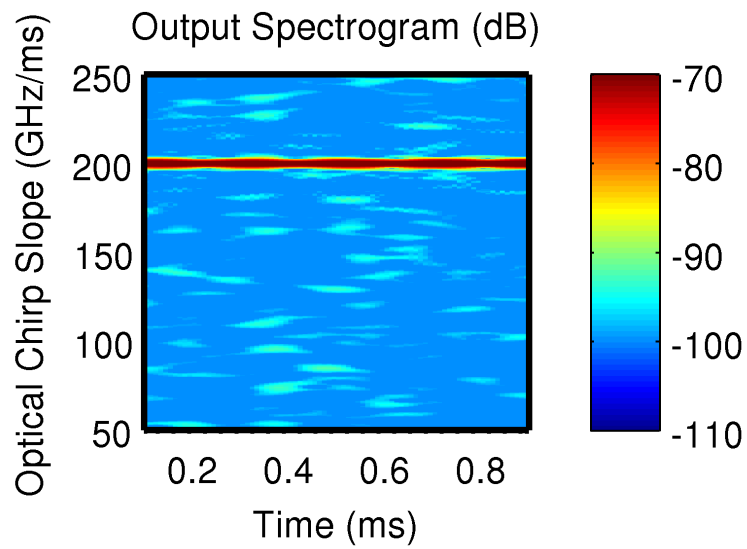
(b)

Figure 6.7. Measured slopes of the (a) input and (b) output optical chirps demonstrating the doubling of the optical chirp slope by FWM.
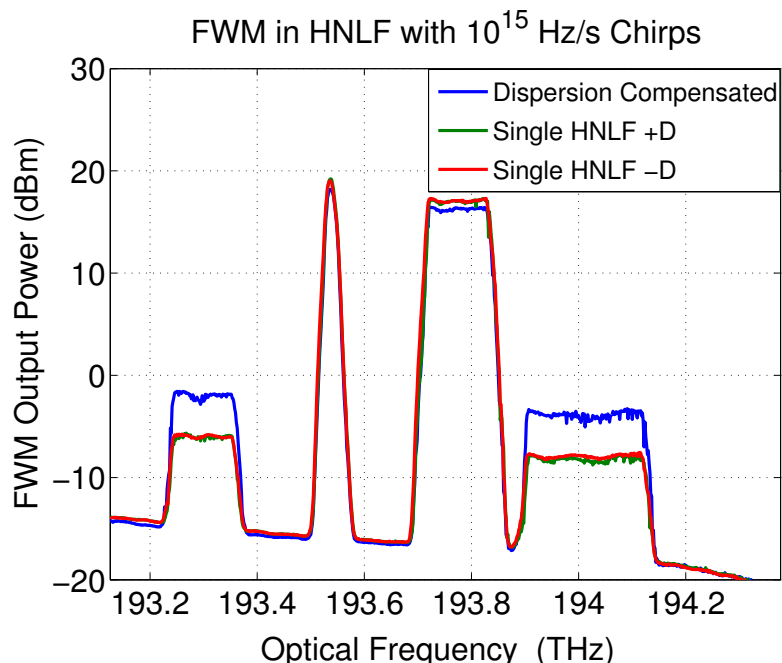
Figure 6.8. Improvement in the power generated by FWM using a two-segment HNLF. The length of each segment was 100 m and the values of the the dispersion parameter in the two segments were +0.38 ps/nm.km (+D) and −0.59 ps/nm.km (-D). The FWM power generated in experiments using the individual 100m HNLF segments is also shown.

dispersion compensated fiber with an input chirp of 100 GHz in 0.1 ms are shown in figure 6.8. An improvement in the conversion efficiency, owing to a longer interaction length for the FWM process, is clearly seen from the figure. If the chirped and reference powers are equal, the theoretical improvement in conversion efficiency is 6 dB; however, the observed improvement is only ∼4 dB, which is due to the slightly lower powers of the chirped and reference waves used.

The output FWM power in this two-segment fiber as a function of the input frequency separation is calculated using equation (B.10) and plotted in figure 6.9. The result is compared to the (hypothetical) case of 200 m of each individual fiber, which results in the same conversion efficiency. The input chirped and reference powers are assumed to be $P_{ch} = P_R = 100$ mW. We note that the bandwidth of the process is improved using the dispersion compensation technique.

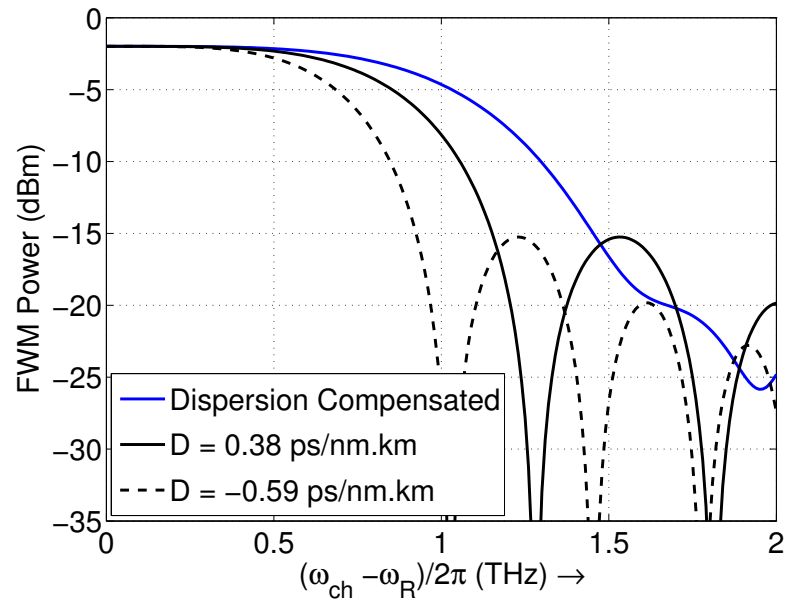As seen from figure 6.9, the low values of the dispersion parameters of the HNLF

Figure 6.9. Theoretically calculated output power as a function of the input frequency difference for the two-segment dispersion compensated HNLF, compared to the same lengths ($L_{tot} = 200$ m) of individual fibers.
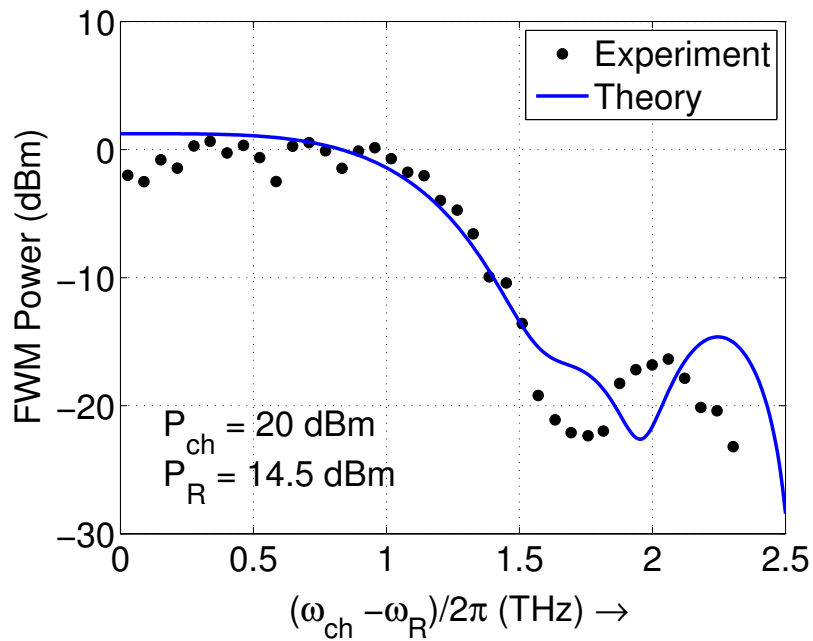

Figure 6.10. Experimentally measured FWM output power as a function of the input frequency difference for a two-segment HNLF, compared to theoretical calculations.

used in the experiment imply that an input frequency separation of the order of 0.5–1 THz is necessary to see a dip in the converted output power. Current implementations of optoelectronic SFLs in our laboratory are limited to bandwidths of ≤0.5 THz, and we therefore use a tunable laser (Agilent) as the chirped laser source in the experimental demonstration. The wavelength of the tunable laser is varied over a range of 2.5 THz, and a VCSEL (RayCan) acts as a monochromatic reference wave. The FWM experiment is then performed using a setup similar to figure 6.5. The nominal powers of the "chirped" wave and the reference wave, after amplification at the input stage, are 100 mW and 28 mW respectively. The actual power deviates from the nominal value due to the nonuniform gain spectrum of the EDFA. The experimentally measured output power as a function of the input frequency difference is plotted in figure 6.10, and compared with the theoretical calculation using equation (B.10). We see that there is good agreement between theory and experiment, and the discrepancies are probably due to the fact that we have assumed average and constant values for the dispersion parameters in each fiber segment, and ignored variations in the powers of the chirped and reference waves.

The effect of dispersion compensation can also be understood by comparing the shape of the roll-off of the power generated by FWM, as a function of the input frequency difference, for the individual fiber segments and the two-segment fiber. As seen in figure 6.11, the shape of the roll-off is almost identical for these fibers, corresponding to a dispersion-limited bandwidth of 100 m of fiber. The power generated is, however, larger by a factor of four in the dispersion-compensated fiber, as seen from figure 6.8.[1]

We have demonstrated the improvement in the bandwidth of the FWM process using a two-segment nonlinear fiber. Preliminary results from experiments with a four-segment fiber confirm the expected improvement in bandwidth; these results will be reported elsewhere.

---

[1]Note that power of the generated FWM wave is normalized in figure 6.11, for low values of $\omega_{ch} - \omega_R$.
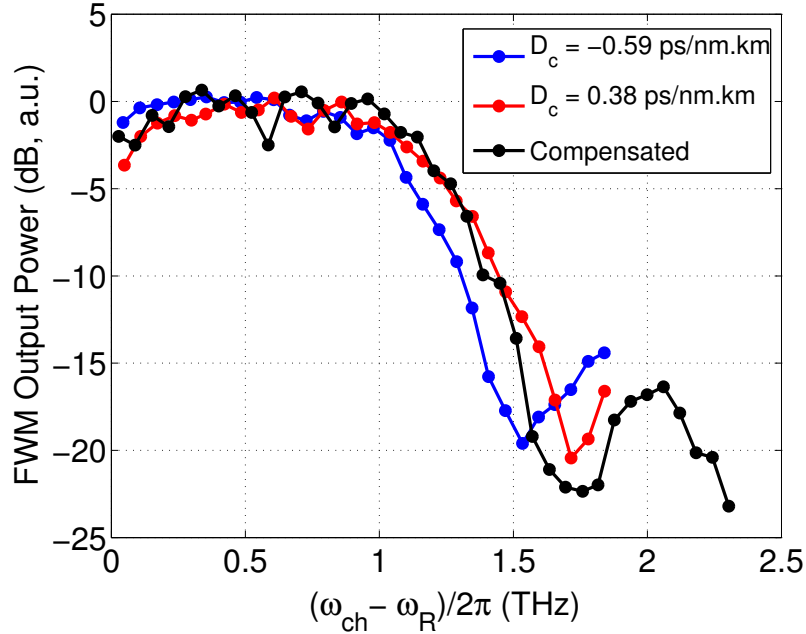
Figure 6.11. Comparison of the normalized experimentally measured FWM power in two individual segments of 100 m each with opposite signs of the dispersion parameter, and the dispersion-compensated two-segment fiber.

6.1.3 Bandwidth Extension

The FWM process demonstrated in this chapter generates a chirp-doubled optical wave in the same wavelength range as the input signal. The frequency spacing between the output chirp and the input chirp is only limited by the sharpness of the optical filter used to filter out the output. Using diffraction grating based filters, this gap can be as small as a few GHz. It has been demonstrated by Ishida and Shibata [128] that the FWM process can be cascaded to geometrically increase the frequency separation between the two input signals. This principle can be extended to chirped signals to achieve geometric increases in the chirp bandwidth. The output chirped signal from the FWM experiment can be filtered, amplified again using an EDFA and mixed with the same reference signal in an HNLF to further double the chirp bandwidth. A cascade of n such stages leads to the geometric scaling of the output bandwidth by a factor 2^n, as shown in figure 6.12. For example, starting with a 200 GHz chirped semiconductor laser at the input, an output bandwidth of 12.8 THz is obtained after
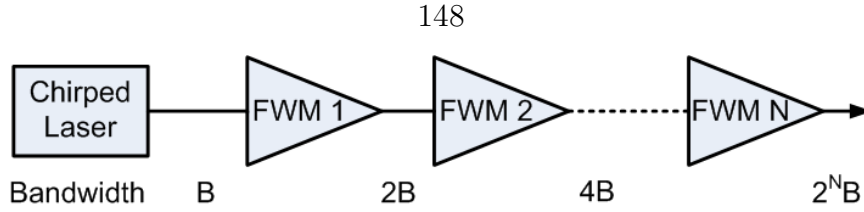
Figure 6.12. Cascaded FWM stages for geometric scaling of the chirp bandwidth. Each stage consists of a coupler, amplifier, HNLF and filter as shown in figure 6.1(a).

$n = 6$ stages. Note that the same reference monochromatic signal can be used for each stage, since the filtering condition (equation (6.6)) is always satisfied if it is satisfied for the first FWM stage. If the dispersion compensation technique for quasi-phase-matching described in section 6.1.1.3 is used, the total output bandwidth is only limited by the gain bandwidth of the amplifiers used in the experiment, and by additional noise introduced by the amplification stages.

The FWM process fundamentally involves the interaction of three input fields to produce the output field. An optimum use of the process for bandwidth multiplication can therefore result in bandwidth tripling, and not just doubling, as described below. Let the monochromatic reference wave of figure 6.1 be replaced by a chirped wave that sweeps in the direction opposite to the original chirp. We now have two input chirped waves which are mirror images of each other, with frequencies given by

$$
\begin{aligned}
\omega_{in,1} &= \omega_0 - B_0 - \frac{d\phi}{dt}, \\
\omega_{in,2} &= \omega_0 + B_0 + \frac{d\phi}{dt},
\end{aligned}
\tag{6.20}
$$

where ω_0 and B_0 are constants. The two output fields generated by two distinct FWM processes have frequencies

$$
\begin{aligned}
\omega_{out,1} &= 2\omega_{in,1} - \omega_{in,2} = \omega_0 - 3B_0 - 3\frac{d\phi}{dt}, \\
\omega_{out,2} &= 2\omega_{in,2} - \omega_{in,1} = \omega_0 + 3B_0 + 3\frac{d\phi}{dt}.
\end{aligned}
\tag{6.21}
$$

The output waveforms have bandwidths that are thrice the bandwidth of the individual input chirps, as shown in figure 6.13. Further, the two output waveforms
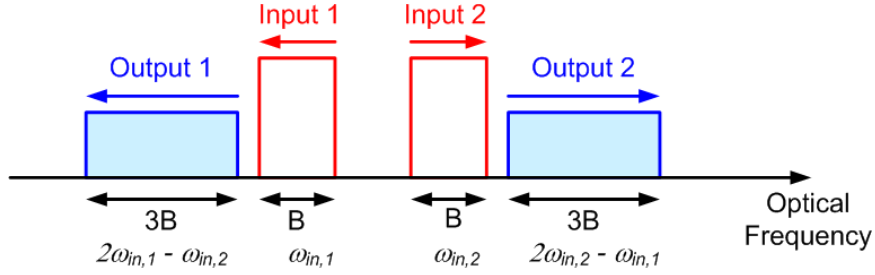
Figure 6.13. Spectral components in a bandwidth tripling FWM experiment using two chirped optical inputs.

can be amplified and used in a cascaded process similar to the one described for the bandwidth-doubling approach, to achieve a geometrical bandwidth scaling of 3^n. Starting with two frequency sweeps of 200 GHz each, a chirp bandwidth of 16.2 THz can now be achieved using $n = 4$ stages.

The geometric enhancement of the chirp bandwidth using a cascade of n stages has the drawback that it requires n amplifiers and n nonlinear waveguides, thereby increasing the overall system cost. This can be overcome by folding back the cascaded process using a FWM "engine" as shown in figure 6.14(a). The input chirped wave sweeps over a bandwidth B during a time T, and is then turned off. A monochromatic reference wave is also coupled into the nonlinear medium. The FWM output of bandwidth $2B$ is selected by the optical filter, delayed by a time T, amplified and fed back into the nonlinear fiber as the chirped input. From time T to $2T$, the optical filter is configured to select the new FWM output of bandwidth $4B$. The combination of optical filter configuration and the delay T therefore ensures that only two optical waves are input into the nonlinear fiber at a given instant of time. The slope of the frequency chirp at the output port then increases geometrically with time, as depicted in figure 6.14(b). The amount of practically achievable delay T imposes a lower bound on the input optical chirp rate, for a given chirp bandwidth. A fiber delay of 20 km provides a delay of 100 μs, which is quite sufficient for sweeping typical semiconductor lasers, and switching the optical filters. This approach can be easily modified to include two chirped inputs.
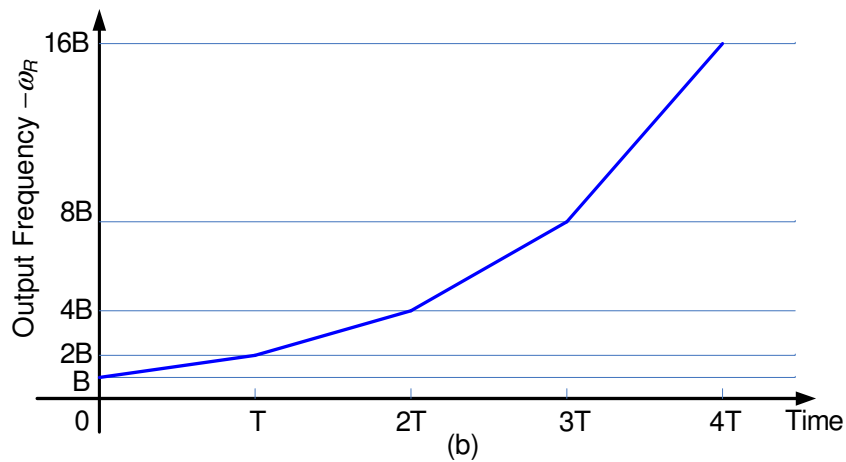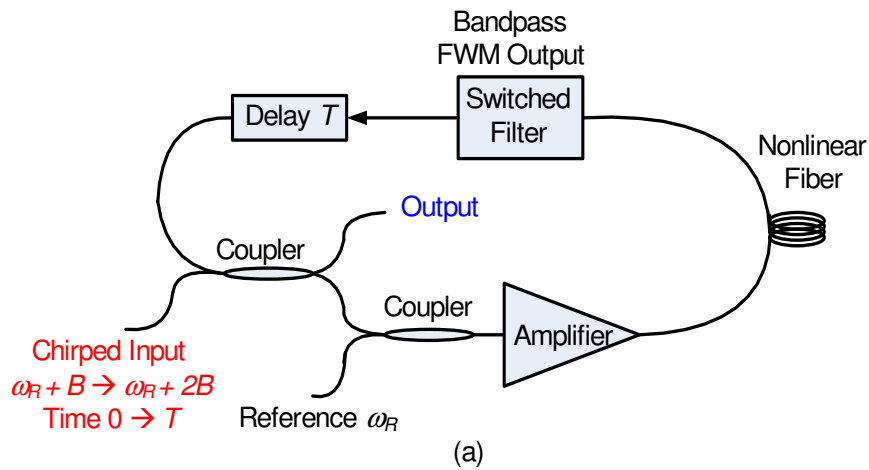
Bandpass
FWM Output

Delay *T*

Switched
Filter

Nonlinear
Fiber

Output

Coupler

Coupler

Amplifier

Chirped Input
$\omega_R + B \rightarrow \omega_R + 2B$
Time $0 \rightarrow T$

Reference ω_R

(a)

16B

8B

4B

2B
B

Output Frequency $-\omega_R$

0

T

2T

3T

4T

Time

(b)

Figure 6.14. (a) FWM "engine" for geometric scaling of the chirp bandwidth. The filter is switched every T seconds so that it passes only the FWM component generated. (b) Output frequency vs. time.

6.2 Multiple Source FMCW Reflectometry

The FWM technique described in section 6.1 relies on a single input chirp and non-linear optics to achieve bandwidth multiplication. This imposes a rather large power requirement, and the achievable bandwidth can be limited by dispersion in the non-linear medium. In this section, we present a new approach, multiple source FMCW (MS-FMCW) reflectometry, which combines multiple lasers so that the total chirp bandwidth to the sum of chirp bandwidths of the individual lasers. This leads to a corresponding decrease in the smallest resolvable feature separation (equation (5.16)) while keeping the ranging depth and scan speed unchanged. The key to this technique is sweeping the sources over distinct but adjacent regions of the optical spectrum, so as to approximate a single sweep of greater bandwidth. A related method for improving the range resolution has recently been reported [129], where the chirped sidebands of the discrete frequencies radiated by a mode-locked laser are combined using feedback to create a phase-coherent continuous-frequency wideband chirp. In contrast, our work focuses on an analytical method that can tolerate the presence of discontinuities in the frequency sweep, enabling a much simpler (and cheaper) combination of multiple sources for resolution improvement.

6.2.1 MS-FMCW Analysis

Let us briefly revisit the FMCW experiment with a linearly swept source of bandwidth B (rad/s), as shown in figure 6.15. The target is assumed to consist of multiple reflections with time delays τ_i. The electric field of the source is given by

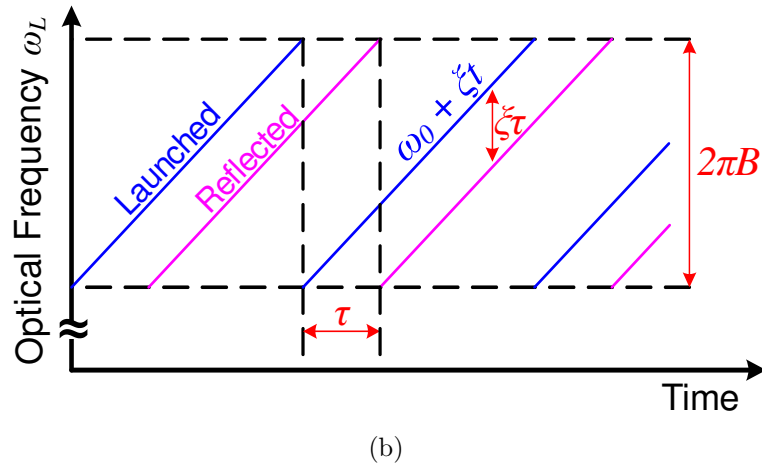$$e(t) = \cos\left(\phi_0 + \omega_0 t + \frac{\xi t^2}{2}\right),\tag{6.22}$$
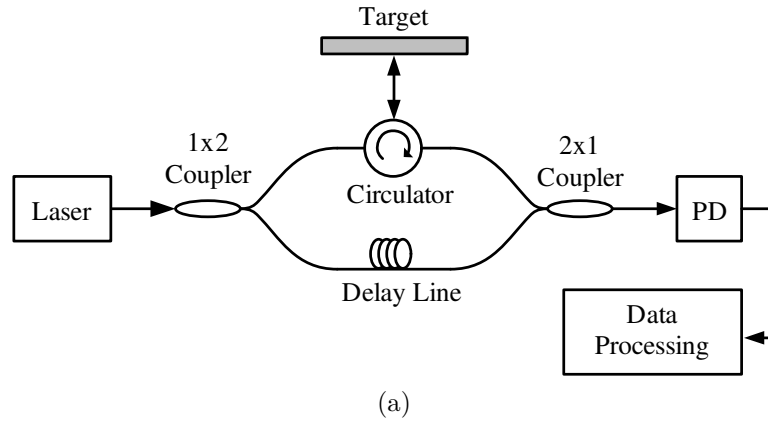
Figure 6.15. (a) Schematic diagram of an FMCW ranging experiment with a linearly chirped optical source. (b) Variation of the optical frequency with time.

where ϕ_0 denotes the initial optical phase. For a target with a time delay τ, the detected photocurrent is given by

$$
\begin{aligned}
i(t) &= \left\langle |e(t) + R\, e(t - \tau)|^2 \right\rangle \\
&= R \cos\left[(\xi\tau)t + \omega_0\tau - \frac{\xi\tau^2}{2} \right],
\end{aligned}
\tag{6.23}
$$

where R is the target reflectivity, and the DC terms are neglected. The averaging is done over a time interval that is much longer than an optical cycle, yet much shorter than the period of the cosine in equation (6.23). The term $\xi\tau^2/2$ is typically much smaller than unity, and will be neglected in the rest of this analysis for the sake of simplicity.[2]

We note that time is only a dummy variable in equation (6.23), and can be replaced by the optical frequency, so that the photocurrent is a function only of the optical frequency:

$$
i(\omega) = R \operatorname{rect}\left(\frac{\omega - \omega_1}{B} \right) \cos(\omega\tau),
\tag{6.24}
$$

where the rect(.) function denotes that the measurement is done over the optical frequency interval of length B centered around ω_1. This is a consequence of the fact that equation (6.23) is valid only for the time interval $[0, T]$. The delay τ is then calculated by measuring the "frequency" of oscillations of the function $\cos(\omega\tau)$, i.e., we define the conjugate Fourier variable, ζ, of the optical frequency ω and calculate the Fourier transform of equation (6.24):[3]

$$
I(\zeta) = \left[\frac{R}{2}\delta(\zeta - \tau) \right] * \left[B\operatorname{sinc}\left(\frac{B\zeta}{2} \right) e^{-j\zeta\omega_1} \right],
\tag{6.25}
$$

where $*$ is the convolution operator, and we ignore negative "frequencies" ζ, since the photocurrent is real. The value of τ is calculated by measuring the location of the peak of the sinc function. Note that one definition of the resolution of the measurement is given by the location of the first null of the sinc function at $\Delta\zeta =$

---

[2]The inclusion of the $\xi\tau^2/2$ term does not change the results of the analysis significantly, as shown in [71].

[3]The Fourier transform of $x(\omega)$ is defined by $X(\zeta) = \int_{-\infty}^{\infty} x(\omega)e^{-j\omega\zeta}\, d\omega$. ζ has units of time.

$2\pi/B$, which corresponds to a range resolution $\Delta d = \pi c/B$, as given by equation (5.16).[4] Alternatively, the resolution may be defined by the FWHM of the sinc function.

We now show that the resolution of the measurement can be improved by simply adding measurements performed using several distinct optical windows. Let the N optical windows be centered at ω_k, and have width B each.[5] We further assume that there is a gap between adjacent windows, so that $\omega_{k+1} - \omega_k = B + \delta_k$. For multiple targets, labeled i, imaged using multiple optical windows, the general version of equation (6.25) can be written as

$$
\begin{aligned}
I(\zeta) &= \left[\sum_i \frac{R_i}{2} \delta(\zeta - \tau_i) \right] * \left[\sum_{k=1}^{N} B\text{sinc}\left(\frac{B\zeta}{2} \right) e^{-j\zeta\omega_k} \right] \\
&\doteq \left[\sum_i \frac{R_i}{2} \delta(\zeta - \tau_i) \right] * A_N(\zeta).
\end{aligned}
\tag{6.26}
$$

$A_N(\zeta)$ can be simplified to yield

$$
\begin{aligned}
A_N(\zeta) = (\omega_N - \omega_1 + B)\text{sinc}\left(\frac{\omega_N - \omega_1 + B}{2} \zeta \right) e^{-j\zeta\frac{\omega_1 + \omega_N}{2}} \\
- \sum_{k=1}^{N-1} \delta_k \text{sinc}\left(\frac{\delta_k \zeta}{2} \right) e^{-j\zeta\left(\omega_k + \frac{B+\delta_k}{2} \right)}.
\end{aligned}
\tag{6.27}
$$

Let us first consider the case $\delta_k = 0$ for all k. This is the case where there are no gaps between the optical windows, and we find that equation (6.27) is identical to equation (6.25) with effective bandwidth $\tilde{B} \doteq \omega_N - \omega_1 + B = NB$. *A resolution improvement by a factor of N can therefore be improved by simply adding measurements taken over N distinct optical windows.*

In the presence of gaps δ_k, the synthesized spectrum in equation (6.27) can be interpreted as the spectrum due to one large window of bandwidth given by *the total frequency extent* $\tilde{B} = \omega_N - \omega_1 + B$, minus the transform of the gaps. In this work,

---

[4]Note that the range resolution is $\Delta d = c\Delta\zeta/2$ owing to the specular reflection geometry used in the experiment.

[5]In general, it is not necessary that the bandwidths B_k be equal.

we will always assume that the gaps are small, i.e., $\delta_k \ll B$. The resolution of the synthesized spectrum can then be exactly calculated numerically as described in [71], but it is easy to show that the FWHM of the transform is virtually unaffected by the presence of small gaps. This is due to the fact that the magnitude of the sum in equation (6.27) is bounded above by $\sum_k |\delta_k|$, and this is, by assumption, much smaller than the total bandwidth $\tilde{B}$ which determines the maximum value of the spectrum. It can also be shown [71] that an upper bound on the smallest resolvable separation is given by

$$\Delta d_{\mathrm{MS-FMCW}} \leq \frac{\pi c}{NB}. \tag{6.28}$$

To illustrate the effect of the gaps on the synthesized spectrum, we plot in figure 6.16 the transform of a single window of width 5.19 units, compared to the addition of five windows of 1 unit each with interwindow gaps of 0.06, 0.045, 0.03 and 0.055 units respectively. It is clear that the resolution of the synthesized measurement is approximately equal to that using a single frequency sweep of 5 units, and the gaps do not have a significant impact on the resolution of the measurement.

6.2.2   Stitching

We now consider the problem of stitching, i.e., how do we put together multiple measurements using different parts of the optical spectrum to obtain one high-resolution measurement? In the previous section, we have mapped photocurrents from the time domain to the optical frequency domain. Since the optical frequency is linear in time, this mapping involves first scaling the time axis by the chirp slope, and then translating the data to the correct initial frequency. Whereas the rate of each chirp is precisely controlled (chapter 5), the starting sweep frequencies are, in general, not known with sufficient accuracy. To reflect this uncertainty, we omit the translation step—in other words, we translate the ideal measurement back to the origin. In the Fourier domain, this implies that the *measured* spectrum using the kth optical window is related to the ideal value by

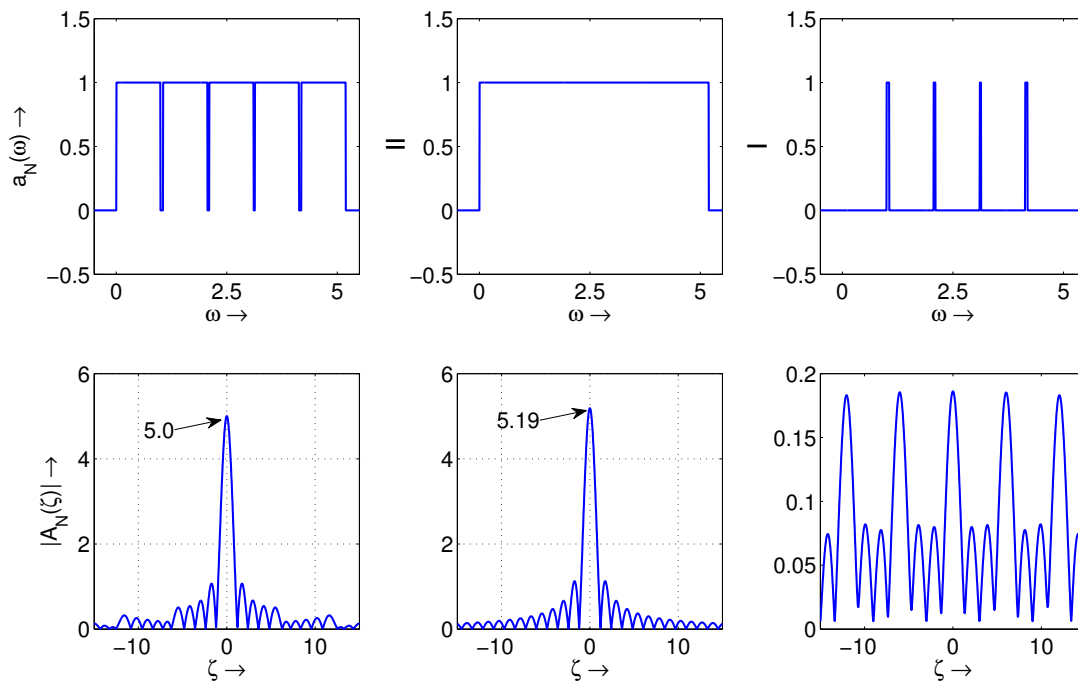$$I_{k,meas}(\zeta) = e^{j\omega_k \zeta} I_k(\zeta). \tag{6.29}$$

Figure 6.16. Illustration of the MS-FMCW concept. A measurement using five individual optical frequency sweeps of one unit each can be regarded as one large sweep minus the gaps between the optical windows. If the sum of the frequency gaps (here, 0.19 units) is much smaller than the total frequency sweep (5.19 units), the resultant bandwidth of the synthesized measurement is at least equal to the sum of the individual bandwidths (5 units).
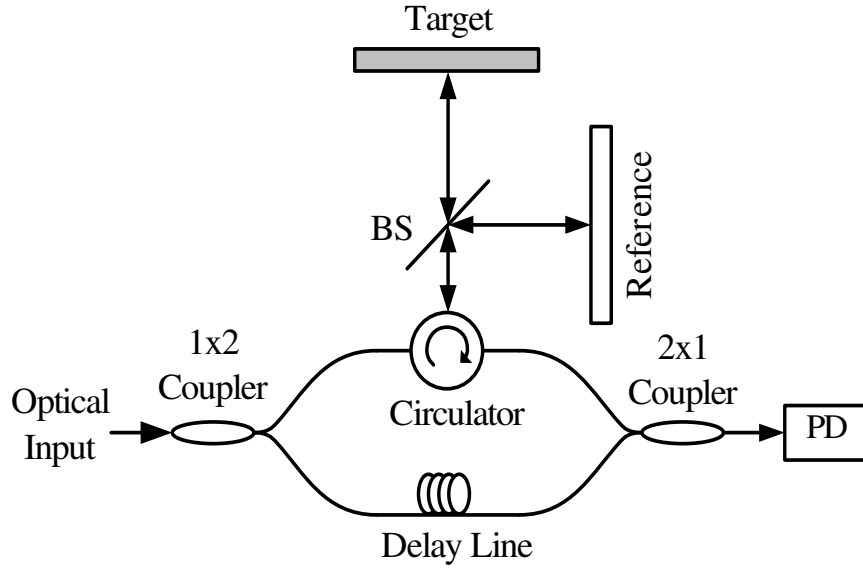
Figure 6.17. Schematic of a multiple source FMCW ranging experiment. A reference target is imaged along with the target of interest, so that the intersweep gaps may be recovered. BS: Beamsplitter. PD: Photodetector.

Using equation (6.25), the measured spectrum is given by

$$
\begin{aligned}
I_{k,meas}(\zeta) &= e^{j\omega_k\zeta}\left[\sum_i \frac{R_i}{2}\delta(\zeta-\tau_i)\right] * \left[B\mathrm{sinc}\left(\frac{B\zeta}{2}\right)e^{-j\zeta\omega_k}\right] \\
&= \frac{B}{2}\sum_i R_i\,\mathrm{sinc}\left(\frac{B(\zeta-\tau_i)}{2}\right)\exp(j\tau_i\omega_k).
\end{aligned}
\tag{6.30}
$$

The problem of stitching is therefore to determine the phase factors $\exp(-j\zeta\omega_k)$ in order to reconstruct the Fourier transform of equation (6.27) according to

$$
I_{stitch}(\zeta) = \sum_{k=1}^{N} e^{-j\omega_k\zeta} I_{k,meas}(\zeta).
\tag{6.31}
$$

The uncertainty in the starting frequencies manifests itself as an uncertainty in the intersweep gaps. To recover the gaps, we use a known reference target along with the target of interest, as shown in figure 6.17. By analyzing the data collected from the reference target, we extract the parameters δ_k, and stitch together the target of interest measurement, according to equation (6.31). Let us examine a system with two optical sweeps of chirp bandwidth B each, separated by a gap δ. Three and more

sweeps can be stitched by considering sweeps in a pairwise manner to calculate the values of the gaps. Suppose the known reference target consists of a single reflector with reflectivity R_a and delay τ_a. We obtain two measurements $I_{1,meas}$ and $I_{2,meas}$ according to equation (6.30). The ratio of these measurements can then be used to obtain the value of the gap δ (note that $\omega_2 - \omega_1 = B + \delta$) according to

$$\delta = \frac{1}{\tau_a} \arg\left[\frac{I_{2,meas}(\tau_a)}{I_{1,meas}(\tau_a)} \exp(-jB\tau_a)\right]. \tag{6.32}$$

The phase of a complex number can only be extracted modulo 2π, so that equation (6.32) can only be used to recover δ with an ambiguity of $2\pi/\tau_a$. Therefore, the nominal gap needs to be known to within $2\pi/\tau_a$ before equation (6.32) may be applied. For example, if the nominal gap is only known to an accuracy of 10 GHz, we need $1/\tau_a > 10$ GHz. However, the use of a very small τ_a is undesirable since it makes the calculation very sensitive to inaccuracies in the measurement of the phase on the right-hand side.

To overcome this issue, we use two known reference reflectors, and express the gap size as a function of the reflector separation. If the two delays are given by τ_a and τ_b, we use equation (6.32) to derive

$$\delta = \frac{1}{\tau_a - \tau_b} \arg\left[\frac{I_{2,meas}(\tau_a)I_{1,meas}(\tau_b)}{I_{1,meas}(\tau_a)I_{2,meas}(\tau_b)} \exp\left(-jB(\tau_a - \tau_b)\right)\right]. \tag{6.33}$$

τ_a and τ_b are chosen so that $1/|\tau_a - \tau_b| > 10$ GHz, and the value of δ is calculated using equation (6.33). The error in this calculation is proportional to $1/|\tau_a - \tau_b|$. The accuracy of the calculation of the gap can now be improved by using equation (6.32), which yields a new value of δ with a lower error proportional to $1/\tau_a$. Depending on system noise levels, more stages of evaluation of δ using more than two reference reflectors may be utilized to achieve better accuracy in the calculations.

A potential system architecture employing the stitching technique for high resolution MS-FMCW is shown in figure 6.18. The optical sources are multiplexed and used to image a target and a reference, as discussed above. The reflected optical signal is
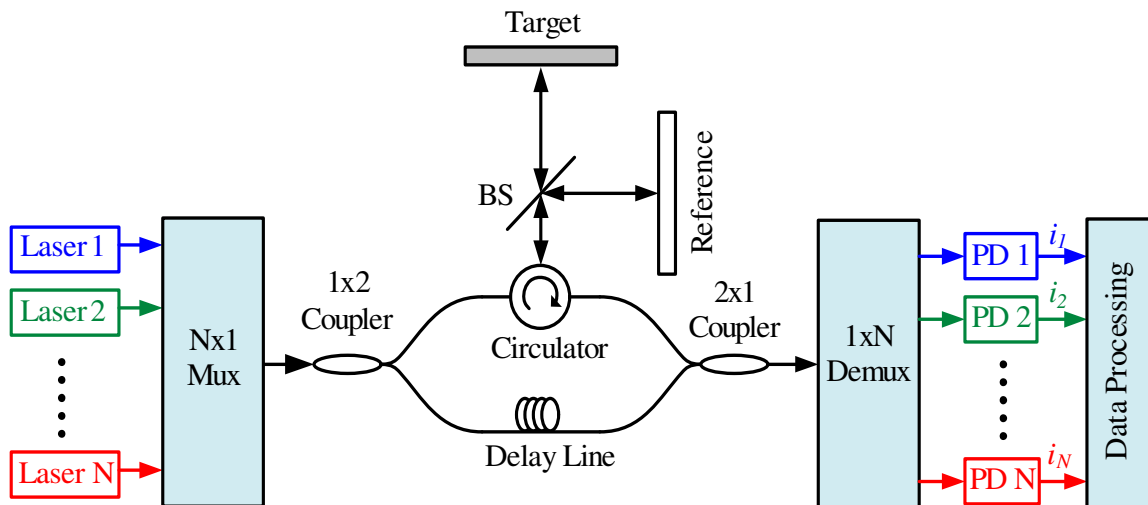
Figure 6.18. Architecture of a potential MS-FMCW imaging system. BS: Beam splitter. PD: Photodetector.

demultiplexed and measured using a set of photodetectors to generate the photocurrents of equation (6.30). The reference data is processed and used to stitch a target measurement of improved resolution. The multiplexing may be performed in time or optical frequency, or a combination of the two. The real power of the MS-FMCW technique then lies in its scalability. We can envision a system that combines cheap off-the-shelf SCLs to generate a swept-frequency ranging measurement that features an excellent combination of range resolution, scan speed, and imaging depth.

6.2.3 Experimental Results

We demonstrated the MS-FMCW technique using a highly linear DFB SCL-based optoelectronic swept-frequency source that chirps 100 GHz around a nominal central wavelength of 1539 nm in a 1 ms long scan (chapter 5). It should be noted that that a specialized source is not necessary for this technique, and chirp nonlinearity may be compensated for by sampling the photocurrent uniformly in optical frequency [51].

We used the configuration of figure 6.17 with a 1.0 mm microscope slide target, and a two reflector reference characterized by $1/|\tau_a - \tau_b| \sim 10$ GHz ($\sim$3 cm free space separation). This reference was chosen to accommodate the accuracy with which the gaps are initially known ($\sim$1 GHz). We tuned the SCL temperature through
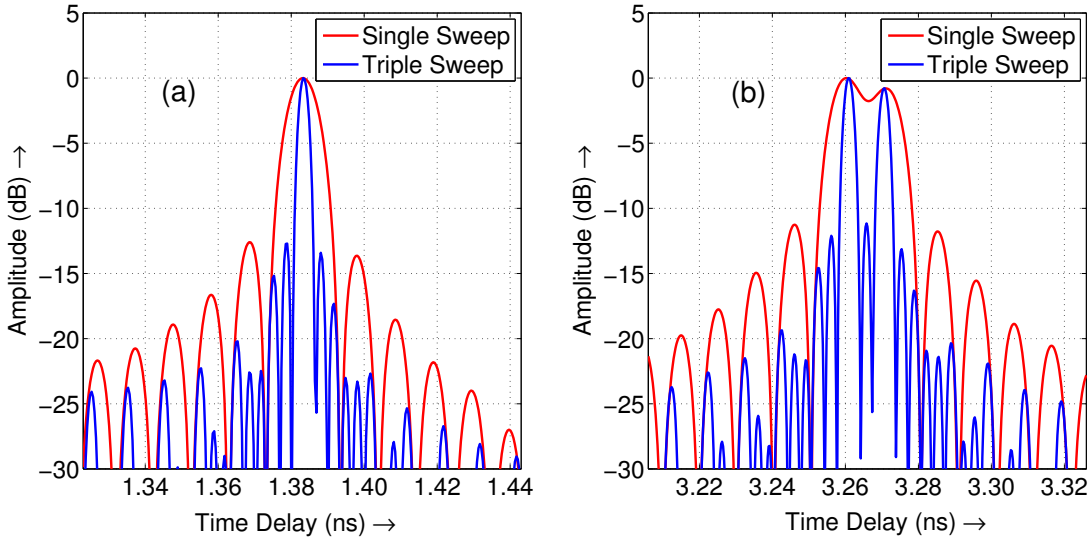
Figure 6.19. Experimental MS-FMCW results using a DFB SCL. The red and blue curves correspond to single-sweep and stitched three-sweep measurements respectively. (a) Single reflector spectrum. (b) Glass slide spectrum. The peaks correspond to reflections from the two air-glass interfaces. The nominal thickness of the glass slide is 1 mm.

three set points to generate three 100 GHz sweeps with different starting frequencies. These sweeps were sequentially launched into the experiment, and the corresponding photocurrents were recorded. Using the two-step procedure described in section 6.2.2, the gaps between the sweeps were calculated to be 1.89 and 0.72 GHz.

These values of the gaps were used in equation (6.31) to stitch the three measured photocurrents, and the results are plotted in figure 6.19. Figure 6.19(a) shows the single sweep and stitched multiple sweep spectra for one of the reference reflectors. The FWHMs are 12.17 and 4.05 ps for the single and multiple source cases respectively. The threefold range resolution enhancement is consistent with equation (6.28). Fig 6.19(b) shows the measurements of the target microscope slide. The two peaks in the single-scan spectrum, corresponding to reflections from the two microscope slide facets, are barely resolved. This is consistent with the theoretical range resolution in glass of 1 mm for a 100 GHz sweep. The stitched curve shows two prominent peaks, demonstrating our improved ability to resolve two closely spaced targets. The measured peak separation of 10 ps is the round-trip delay between the two slide facets,

and indeed corresponds to a thickness of 1 mm in glass.

The stitching experiment was also performed using a VCSEL-based optoelectronic SFL with a chirp bandwidth of 500 GHz, corresponding to a range resolution of 200 µm in glass. Two such sweeps were generated by biasing the laser at different temperatures, and the resulting measurements were stitched together to obtain an effective chirp bandwidth of 1 THz and a resolution of 100 µm in glass. The results of imaging measurements of two-reflector targets with different separations is shown in figure 6.20. The results show that a microscope cover-slip of nominal thickness 150 µm, which could not be resolved by a single sweep, is well resolved by the stitched measurement.

6.2.4   Summary

We have analyzed and demonstrated a novel variant of the FMCW optical imaging technique. This method combines multiple lasers that sweep over distinct but adjacent regions of the optical spectrum in order to record a measurement with increased effective optical bandwidth and a corresponding improvement in the range resolution. The MS-FMCW technique is scalable and is a promising approach to realize a wide-bandwidth swept-frequency imaging system that inherits the speed and coherence of the SCL. While we have demonstrated the stitching of three 100 GHz sweeps using DFB SCLs and two 500 GHz sweeps using VCSELs in our proof-of-concept experiments, MS-FMCW reflectometry is not tied to any particular laser type and may be used to combine wideband swept sources to push range resolutions beyond the state of the art.
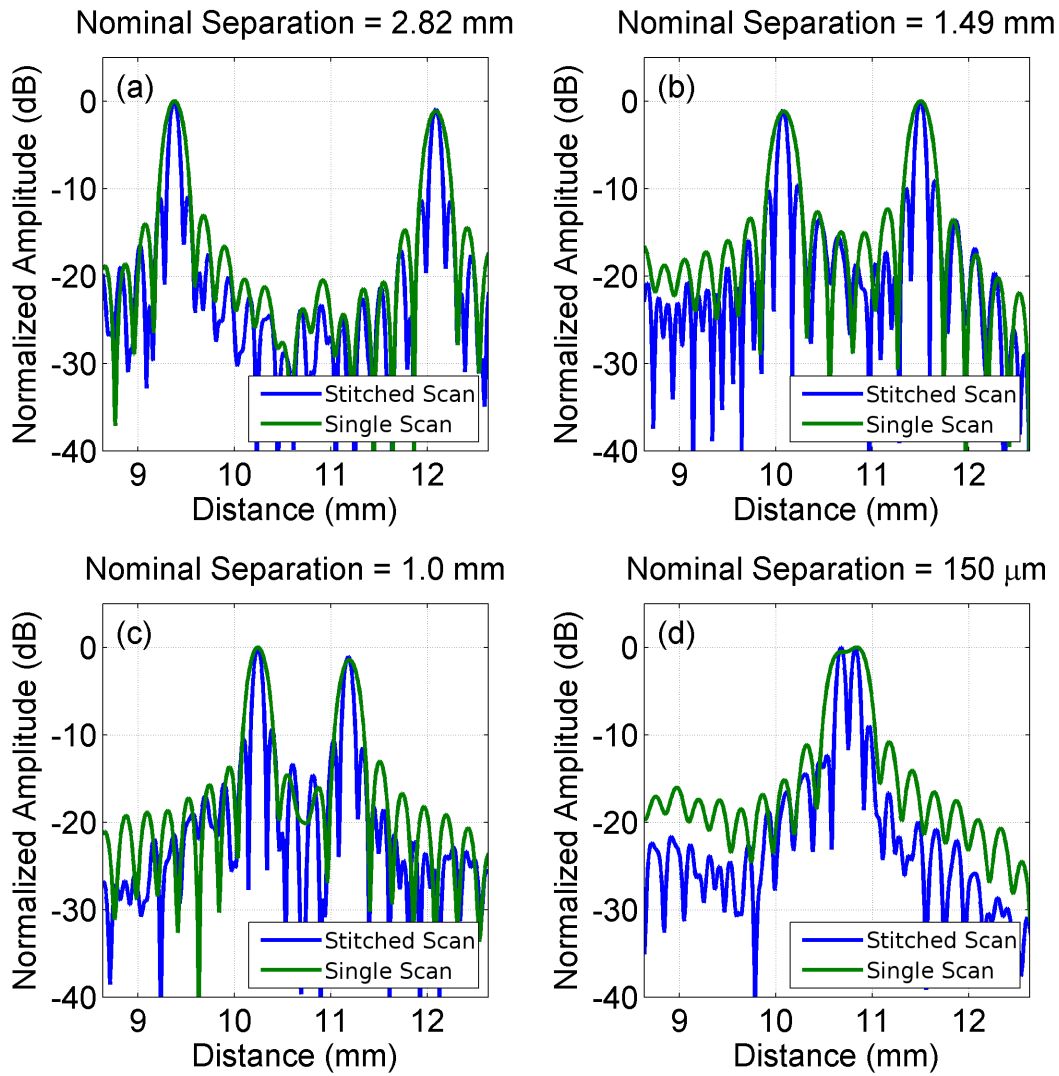
Figure 6.20. Experimental MS-FMCW results using a VCSEL. The green and blue curves correspond to single-sweep and stitched two-sweep measurements respectively.